

Propagation and Dynamics of Relativistic Jets

Akira Mizuta¹, Shoichi Yamada², and Hideaki Takabe¹

amizuta@ile.oksaka-u.ac.jp

ABSTRACT

We investigate the dynamics and morphology of jets propagating into the interstellar medium using 2D relativistic hydrodynamic simulations. The calculations are performed assuming axisymmetric geometry and trace a long propagation of jets. The jets are assumed to be 'light' with the density ratio between the beam to the ambient gas much less than unity. We examine the mechanism for the appearance of vortices at the head of jets in the hot spot. Such vortices are known as a trigger of a deceleration phase which appears after a short phase in which one dimensional analysis is dominant. We find that an oblique shock at the boundary rim near the end of the beam strongly affects the flow structure in and around the hot spot. Weakly shocked gas passed through this oblique shock and becomes a trigger for the generation of vortices. We also find the parameter dependence of these effects for the propagation and dynamics of the jets. The jet with slower propagation velocity is weakly pinched, has large vortices and shows very complex structure at the head of the jets and extended synchrotron emissivity.

Subject headings: galaxies: jets — hydrodynamics – shock waves – methods: numerical — relativity

1. INTRODUCTION

It is widely known that there are three classes of highly collimated and supersonic jets from dense central objects with accretion disks. Depending on the central object the following can be distinguished : protostars, binary stars, and Active Galactic Nuclei (AGN). AGN jets are the largest scale phenomena and the velocity of the jet beam is highly relativistic, at

¹Institute of Laser Engineering, Osaka University, 2-6 Yamada-Oka, Suita, Osaka, 565-0871, JAPAN

²Department of Physics, Waseda University, Okubo, Shinjuku, Tokyo, 169-8555, JAPAN

least close to the central objects (see for example, Pearson et al. (1981); Biretta, Sparks, & Macchetto (1999)). The jet, which originates near an accretion disk that surrounds an AGN, can propagate over a long distance up to a few Mpc while remaining well collimated. There are two shocks at the end of the jet. One is a bow shock (or a forward shock) which accelerates the ambient gas. The other is a terminal Mach shock (or a reverse shock) at which the beam ends. At the terminal Mach shock, non-thermal particles are accelerated and emit photons due to synchrotron radiation and inverse Compton scattering. The gas which crosses the terminal Mach shock into a hot spot is hottest and pressurized and then expands laterally and envelops the beam with the shocked ambient gas, creating a so-called cocoon structure. At the contact discontinuity between the ambient gas and the jet in the cocoon Kelvin-Helmholtz instabilities develop.

Cygnus A is a suitable object to see these features because it is one of the closest radio galaxies and the beam propagates to perpendicular direction to line of sight. From observations, its size is about 120kpc, the beam velocity is $0.4 \sim 1c$ and the hot spot's ram pressure advance speed is $0.03c$ (Carilli et al. 1998), where c is the speed of light. For more details of AGN jets, see for example Carilli & Barthel (1996); Ferrari (1998); Livio (1999) and references therein.

Other active regions in jets are knots and secondary hot spots. Some knots with non-thermal emission can be seen sporadically along the straight beam flow. The emissivity between the knots varies even if they belong to the same jet. Recent high resolution observations of AGN jets show fine structure of knots in the beam flow for up to several tens of kilo parsecs in M87 (Biretta, Sparks, & Macchetto 1999; Marshall et al. 2002; Wilson & Yang 2002), 3C273 (Bahcall et al. 1995; Marshall et al. 2001; Sambruna et al. 2002; Jester et al. 2002), the jet in Centaurus A (Kraft et al. 2002), 3C 303 (Kataoka et al. 2003), and others (Sambruna et al. 2001). Knots on sub-parsec or parsec scales are thought to be due to intermittent flows from the central source and knots in 'blazars' are due to exceptionally strong shocks which are caused by the collisions of internal shocks (Spada, Ghisellini, Lazati, & Celotti 2001; Bicknell & Wagner 2002). Knots on kilo parsec or larger scales are not well understood. The high energy particles that are accelerated on parsec scales may retain their energy for a long time. In some jets, one observes secondary hot spots adjacent to the primary hot spot at the head of jets. The emissivity of secondary hot spot can be as high as that of primary hot spot. It is thought that the gas in the secondary hot spot is separating from the primary hot spot. For example, at both eastern and western side of Cygnus A jet, a bright secondary hot spot is observed (Wilson & Yang 2000). The reason for these multiple hot spots is not well understood.

Recent observations of AGN jets provide information not only about the features of

large scale jets but also that of very small scale jets such as in ‘Compact Symmetric Objects’ (CSOs) which are believed in the first stage of AGN jets from its morphology. CSOs show two sided emissivity within the central few kpc of its parent galaxy. The physical properties of two hot spots and lobes at both sides have been measured (Owsianik & Conway 1998; Polatidis & Conway 2003; Giroletti et al. 2003). CSOs are only a few thousand years old. and the propagation velocity of the hot spot is a few tens of percent of the speed of light. CSOs may tell us about the physical conditions during the earliest phases of jets.

To understand the morphology and the dynamics of the jet, analytical studies and numerical simulations have been performed for the past thirty years. Blandford & Rees (1974) and Scheuer (1974) discussed the structure of the jet with the relativistic beam model theoretically. Some of the early numerical work was done by Norman et al. (1982). Although these were non-relativistic simulations, they showed the main structure of jets, that is two shocks at the head of the jet and the cocoon. The difficulty of numerical relativistic hydrodynamics has delayed the investigation of the relativistic effects on the morphology and the dynamics of jets. Only since the past ten years stable codes with or without external magnetic fields have been developed for the ultra-relativistic regime (Eulderink & Mellema 1995; Duncan & Hughes 1994; Font et al. 1994; Koide, Nishikawa, & Mutel 1996; Komissarov 1999; Aloy et al. 1999a; Hughes, Miller, & Duncan 2002). which allowed the investigations of the formation, collimation, and propagation of jets (Rosen et al. 1999; Koide et al. 2002)

Martí et al. (1997) and Aloy et al. (1999b) performed long term simulations to study the morphology of the jets with 2D and 3D relativistic hydrodynamic codes. Propagation of the relativistic jets in the external magnetic field were computed by Komissarov (1999). These studies verified that the morphology of jets depends on a number of dimensionless parameters: the density ratio of the jet beam to the ambient gas ($\eta \equiv \rho_b/\rho_a$), Lorentz factor of the beam, and the Mach number of the beam ($M_b = v_b/c_{s,b}$). Here the subscripts ‘b’ and ‘a’ stand for beam and ambient gas, respectively. In most of these simulations, a pressure matched jet is assumed, with the pressure ratio $K \equiv p_b/p_a = 1$. Martí, Müller, & Ibañez (1998) performed long term simulations of jets and found a deceleration phase of the propagating jets. Recently Scheck et al. (2002) have pointed out that the propagation velocity, v_j^{1D} , which is derived from one dimensional momentum balance at the rest frame of the contact discontinuity is very useful for understanding the propagation of the jet into the ambient gas. They assumed a constant velocity $v_j^{1D} = 0.2c$ and the kinetic luminosity of the beam is fixed to be $L_{kin} = 10^{46} \text{erg s}^{-1}$ in their models. Those are the first numerical simulations using relativistic hydrodynamic code which assume the propagation efficiency v_j^{1D}/v_b is less than 0.5 (cf. most numerical simulations done so far assume the efficiency is $0.5 \sim 1$). Thus more wide range of parameter space of v_j^{1D} is necessary if we agree with recent observations of CSOs are young AGN jets. Scheck et al. (2002) also investigated

the dependence of the composition of jets using a generic equation of state. They varied the density ratio (η), pressure ratio (K), Mach number (M_b) and the fraction of protons, electrons, and positrons in their three models. The main difference between the various models is seen in the radiative properties of the jets. The deceleration phase is also confirmed and shown to begin with the generation of a large vortex at the head of jet. It seems indeed consistent with observations that jets have a deceleration phase because CSOs have a propagation speed of a few tens percent of the speed of light, while in large scale jets such as Cygnus A the velocity is only a few percent of speed of light. However the physics of the generation of vortices is not well understood.

A first attention to compare the vortex structures in numerical simulations of the jets with observational data have been made by Saxton et al. (2002); Saxton, Bicknell, & Sutherland (2003). who discussed the shock structures at the head of the jet of Pictor A and rings in the cocoon of Hercules A. We note that radio jets with such features are rare (Gizani & Leahy 2003).

In this paper we will examine the mechanism that causes such vortices in some detail. We present three simulations with different v_j^{1D} as injected beam conditions. We pay special attention to the generation of vortices in the hot spot and the separation of vortices from hot spots which strongly affects the dynamics of jets. We show the mechanism of generation of vortices at the head of jet. We hope that this study will help us to better understand the propagation of jets into the ambient gas. This paper is organized as follows. In Sect. 2, the basic equations are presented. In Sect. 3, we show our three models for the numerical numerical simulations. The results and discussion are shown in sect. 4. The surface brightness of synchrotron emissivity and the resolution study are also shown. The conclusion is given in Sect. 5.

2. BASIC EQUATIONS

2.1. RELATIVISTIC HYDRODYNAMIC EQUATIONS

Relativistic flows, $v \sim 1$, affect the morphology and dynamics of jets. The relativistic hydrodynamic equations (Landau & Lifshitz 1987) then have to be solved:

$$\frac{\partial(\rho W)}{\partial t} + \frac{1}{r} \frac{\partial r(\rho W v_r)}{\partial r} + \frac{\partial(\rho W v_z)}{\partial z} = 0, \quad (1)$$

$$\frac{\partial(\rho h W^2 v_r)}{\partial t} + \frac{1}{r} \frac{\partial r(\rho h W v_r^2 + p)}{\partial r} + \frac{\partial(\rho h W^2 v_r v_z)}{\partial z} = \frac{p}{r}, \quad (2)$$

$$\frac{\partial(\rho h W^2 v_z)}{\partial t} + \frac{1}{r} \frac{\partial r(\rho h W^2 v_r v_z)}{\partial r} + \frac{\partial(\rho h W^2 v_z^2 + p)}{\partial z} = 0, \quad (3)$$

$$\frac{\partial(\rho h W^2 - p)}{\partial t} + \frac{1}{r} \frac{\partial r(\rho h W^2 v_r)}{\partial r} + \frac{\partial(\rho h W^2 v_z)}{\partial z} = 0, \quad (4)$$

where, ρ, p, v_i, W , and h are rest mass density, pressure, three velocity component in i direction, Lorentz factor ($\equiv (1 - v^2)^{-1/2}$), and specific enthalpy ($\equiv 1 + \epsilon + p/\rho$), respectively. In this section we equate the velocity of light to unity. We assume axisymmetry. The set of equations (1-4) is not closed until the equation of state is given. In this paper we assume an ideal gas;

$$p = (\gamma - 1)\rho\epsilon, \quad (5)$$

where γ and ϵ are a constant specific heat ratio and specific internal energy, respectively.

2.2. PROPAGATION VELOCITY

A one dimensional analysis is useful for estimating the propagation velocity of the jet. Here the propagation velocity v_j is defined to be the velocity of the contact discontinuity at the end of the jet in the rest frame of the ambient gas. For very 'light' jets ($\eta \ll 1$), in general, the propagation velocity is less than that of the beam because the conversion of the large fraction of the beam kinetic energy to the thermal energy occurs at the terminal Mach shock.

2.2.1. NON RELATIVISTIC CASE

If the velocity and temperature of the gas are in the non-relativistic regime, it is sufficient to consider the Euler equation. Assuming momentum balance in the rest frame of contact discontinuity,

$$S_b (\rho_b (v_b - v_j^{1D})^2 + p_b) = S_a (\rho_a (-v_j^{1D})^2 + p_a), \quad (6)$$

where S_b and S_a are the cross section of the beam and the hot spot, and v_j^{1D} is the propagation velocity derived from one dimensional analysis. Solving Eq.(6) for v_j^{1D} , we obtain

$$v_j^{1D} = \frac{A\eta v_b - \sqrt{A^2\eta^2 v_b^2 - (A\eta - 1)(A\eta v_b^2 + (AK - 1)c_{s,a}^2/\gamma)}}{A\eta - 1}, \quad (7)$$

where c_s is sound speed and A is cross section ratio ($A \equiv S_b/S_a$). If we can assume $A = 1$ and neglect the term that includes $K(\equiv p_b/p_a)$ in Eq.(6), then this equation reduces to

$$v_j^{1D} = \frac{\sqrt{\eta}}{\sqrt{\eta} + 1} v_b. \quad (8)$$

This is the same as the equation derived by Norman, Winkler, & Smarr (1983) for the pressure matched jet ($K = 1$). If the density ratio η is much less than unity, in the case of ‘light’ jet, the propagation efficiency defined as v_j/v_b is much less than unity.

2.2.2. RELATIVISTIC CASE

For the relativistic case, assuming again 1D momentum balance between the beam and the ambient gas in the rest frame of the contact discontinuity at the head of the jet,

$$S_b (\rho_b h_b W_j^2 W_b^2 (v_b - v_j^{1D})^2 + p_b) = S_a (\rho_a h_a W_j^2 (-v_j^{1D})^2 + p_a), \quad (9)$$

where $W_j = (1 - v_j^{1D2})^{-1/2}$. This equation leads to

$$v_j^{1D} = \frac{A\eta_R^* v_b - \sqrt{A^2 \eta_R^{*2} v_b^2 - (A\eta_R^* - 1)(A\eta_R^* v_b^2 + (AK - 1)c_{sa}^2/(\gamma W_j^2))}}{A\eta_R^* - 1}, \quad (10)$$

$$\text{with } \eta_R^* \equiv \eta_R W_b^2, \quad \eta_R \equiv \frac{\rho_b h_b}{\rho_a h_a}. \quad (11)$$

In general, the sound speed of interstellar matter is much smaller than the velocity of the beam ($c_{s,a} \ll v_b$) so we can neglect the term including K . As a result, Eq.(10) becomes

$$v_j^{1D} = \frac{\sqrt{A\eta_R^*}}{1 + \sqrt{A\eta_R^*}} v_b. \quad (12)$$

This is equal to the equation derived by Martí et al. (1997) for the pressure matched jet ($K = 1$) if we assume $A = 1$. Scheck et al. (2002) showed that the time evolution of the actual propagation velocity is almost the same in their models for fixed v_j^{1D} and $A = 1$, in spite of the large variation of the specific internal energy of the beam during the first phase. There are several ways to explain the deceleration of jets between sub parsec and mega parsec scales. If the density ratio η varies, η should become smaller than that in the earlier phase. The Lorentz factor should also become smaller. The velocity at the head of the beam should be relativistic to reproduce strong emissivity at the hot spot. The effect of the Lorentz factor seems small. Another possibility is variation of the density profile of the ambient gas. For example, it is natural to assume that the ambient gas decreases in density as function of distance from the AGN. In the models of Scheck et al. (2002), the multidimensional effect, namely decreasing cross section’s ratio, becomes very important for the dynamics and the jet decelerates gradually. Scheck et al. (2002) compared the time evolution of the dynamics with the extended Begelman-Cioffi model. The original model derived by Begelman & Cioffi (1989) assumes a constant propagation velocity and Scheck et al. (2002) extended the assumption to a power law.

3. NUMERICAL CONDITIONS

We solve the relativistic hydrodynamic equations Eq.(1-5) with a 2D relativistic hydrodynamic code recently developed by one of the authors (A.M.). The detailed numerical method and test calculations of the code are given in the appendix of this paper.

We use a 2D cylindrical computational region $r \times z$. The grid size in both r and z directions is uniform, namely $\Delta r = \Delta z = \text{const}$. We assume that the ambient gas is homogeneous initially. Calculations including clouds in the ambient gas have been made by de Gouveia Dal Pino (1999); Zhang, Koide, & Sakai (1999); Hughes, Miller, & Duncan (2002). A relativistic beam flow (v_b) which is parallel to z axis is continuously injected from one side of the computational region ($z = 0$). The inner 10 grid points from the symmetry axis are used for this. The radius of the injected beam $R_b = 10\Delta r$ is used as a scaling unit in this study. The computational region covers $50R_b(r) \times 180R_b(z)$; corresponding to a grid 500×1800 grid. The radius of the beam near the central engine is unknown, and we assume a plausible value of $1R_b = 0.5\text{kpc}$, corresponding to $25\text{kpc} \times 90\text{kpc}$ for the computational region. A free outflow condition is employed at the outer boundaries for $r = 50R_b$ and $z = 180R_b$. A reflection boundary is imposed on the symmetry axis as well as at $z = 0$ with $r > R_b$. The boundary condition at $z = 0$ is crucial for dynamics and the outer shape of the jets. The free boundary condition permits the gas to escape at the back side (Saxton et al. 2002). According to observations jets have counter jets which propagate in the opposite direction. We assume the reflective boundary condition so that our calculations begin near central engine.

We examine three injection beam conditions (Table 1) with different v_j^{1D} . The description of v_j^{1D} is given in Eq.(12), here $A = 1$ is assumed. The beam velocity is fixed to $v_b = 0.99c$ (the corresponding Lorentz factor is $W_b = 7.1$). The Mach number of the beam is also fixed to $M_b = 6.0$. We assume that the beams don't have highly relativistic temperatures and that remains constant v_b . As a result v_j^{1D} depends only on the density ratio η . Scheck et al. (2002) adopted $v_j^{1D} = 0.2c$ as the injected beam conditions for their calculations. This is in the range of acceptable propagation velocity based on observation of CSOs. We explore the region of the propagation velocity v_j^{1D} from $0.2c$ to $0.4c$ and investigate the dependence of the difference of v_j^{1D} caused by different η . With increasing v_j^{1D} , η varies about a factor of ten; from 1.28×10^{-3} to 9.15×10^{-3} . We label these cases JB02, JB03, and JB04, and the corresponding v_j^{1D} are $0.2c$, $0.3c$, and $0.4c$. Although there is only about one order difference in the density ratio for all beams, doubling value of v_j^{1D} has a big effect on the dynamics of jets and their long term propagation. Because the spatial scale is fixed, we adopt different expiration times for each models, see Table 1 again.

The initial rest mass density of ambient gas ρ_a is unity for all models. The pressure

ratio(K) is chosen to be from $K = 10$ to 100 so that the ambient gas is approximately similar in all cases. As a result, the temperature of the ambient gas for all injected beams is a few eV, if we assume the ambient matter is pure hydrogen gas.

Because we choose similar values of v_j^{1D} to those of Scheck et al. (2002), other parameters (η, K, M_b) are also very similar.

4. RESULTS AND DISCUSSION

4.1. MORPHOLOGY AND DYNAMICS

From our simulations, we find that the overall morphology and dynamics of the jets are similar to that discussed in previous work. Figures 1, 2 and 3 show snapshots of rest mass density, pressure, and Lorentz factor for three models near the end of the simulations, $t = 1770[R_b/(c)]$ (model JB02), $t = 1140[R_b/(c)]$ (model JB03) and $t = 570[R_b/(c)]$ (model JB04). Since these jets have different beam conditions, the end times are also different as discussed in the previous section. However this is not only due to different v_j^{1D} values, but also because of differences in deceleration phase of the jets which are caused by the generation and separation of vortices at the head of the jet, as we will discuss later. At first glance, the outer shapes of the jets are quite different. Model JB02 shows a conical outer shape which is very similar to the results found by Scheck et al. (2002). This is not seen in the other two models (JB04 and JB03). All beams remain collimated from $z = 0$, where the beam is injected into the computational region, to the head of the jets. It is also important to note that the beam radius does not increase monotonically from the source to the head of jets. At the head of the jet the radius of the beam is $3 \sim 5R_b$. The opening angle is very small $1^\circ \sim 2^\circ$ for all models. High Lorentz factors exist only along the z axis in the beam flow, but they do vary. That means that a large part of the injected kinetic energy is transported from the central engine to the head of the jet along the beam flow. At the end of the beam a strong 'terminal Mach shock' can be seen. One of the most active points is called a 'hot spot' into which shocked beam gas enters through the terminal Mach shock at the head of the jet. The pressure in the hot spot is very high due to the energy dissipation at the terminal Mach shock and is matched by ambient gas compressed at the bow shock. Moderate Lorentz factors ($W \sim 2$) exist in the cocoon. These are due to back flows that begin at a hot spot and flow back in the center of the cocoon parallel to the beam flow. This mildly relativistic back flow seems a little strange thing because the head is proceeding very slow ($\lesssim 0.2$) and the expanding velocity from the hot spot is up to $0.5c$ in the comoving frame (maximum sound speed). It should be noted that this mildly relativistic backflow is longer for slower jets. Thus some acceleration mechanism or other effects are necessary.

We discuss this in the next subsection. This back flow creates a shear flow and the contact surface becomes unstable due to Kelvin-Helmholtz instabilities. The surface between the back flow and shocked ambient gas's flow also becomes unstable and causes the appearance of vortices in the larger cocoon.

To understand the difference of these models after long term propagation we must study the dynamics of the jets. Figure 4 shows the time evolution of the positions of the contact discontinuity, the bow shock (forward shock), and the terminal Mach shock (reverse shock) at the head of the jet for each model. Three straight lines which correspond to the lines of one dimensional analysis are also shown for the comparison. It is difficult to define the positions of these surfaces because of the complex structure at the head of the jets. In this paper we show the positions at $r = 0$, namely along the z axis. It is hard to identify the contact discontinuity between shocked ambient gas and shocked beam gas especially in later phase because of mixing of the shocked beam with the ambient gas due to the generation of vortices. The contact discontinuity is defined as the boundary of shocked ambient gas that has half the maximum density. We plot the points where the Lorentz factor becomes 2 at the head of the jet. The two phases indicated by Martí, Müller, & Ibañez (1998) and Scheck et al. (2002) are also seen in our results. During the first phase, all of the slopes are constant. Model JB02 has a propagation velocity $\sim 0.2c$ and the one dimensional analysis discussed in section 2.2 is in good agreement with our result. For JB03 and JB04 the propagation velocity is a little faster than that of in our one dimensional estimates. During first phase the surfaces are very close each other. On the other hand, in the second phase, the surfaces separate and approach each other repeatedly. The propagation velocity is no longer constant and the jet is decelerating gradually. Some vortices grow at the head of jet and separate towards the back side. This affects the dynamics of the jets.

Figure 5 shows snap shots of the velocity ($\sqrt{v_r^2 + v_z^2}$) during the earlier phase of the each models. Although its path is not as straight as that of the beam, the back flow does remain parallel to the beam flow. The back flow velocities are very similar for all models ($0.3 \sim 0.4c$). Because the propagation velocity is less than that of back flow for the model of JB02, most of it reaches the boundary, after which some of the gas expands in lateral direction, and other gas form a new flow which is between the beam and the back flow. This new flow also can be seen in the case of JB03 near the boundary, but it does not reach the head of jet like JB02 because the propagation velocity is faster than that of JB02. The beam flow and back flow lie side by side in the model JB03 and JB04 near the head of the jets.

In later phases this 'third' flow, which is not beam flow but has the same propagating direction, exists in all models because of vortices generated in the cocoon due to Kelvin-Helmholtz instabilities. At this stage the back flow becomes very complex. How much gas

reaches the boundary at $r = 0$ affects the expansion into lateral directions for each model. Slower propagation velocities result in cone like outer shapes of the jets. The shocked ambient gas forms a shell-like structure like a football, resembling the observed X-ray emission Cygnus A by *Chandra* (Wilson & Yang 2000). It is consistent with our results because the present propagation velocity of Cygnus A is very small ($\sim 0.03c$). A long time may have passed after the deceleration phase began in the Cygnus A jet. In contrast, in models JB03 and JB04, which have propagation velocities faster than that of the back flow in the earlier phase do not have a conical shape. These jets are decelerating. The effect of a decreasing propagation velocity can be seen near the head of the jet in JB03, showing a conical shape around the head of the jet.

4.2. VORTEX FORMATION IN HOT SPOTS

We discussed the generation and separation of large vortices at the head of the jet which occurs repeatedly during the second phase. Such processes strongly affect the dynamics of jets and was also found by Scheck et al. (2002). It is also consistent with observations between the high speed CSO sources and slower large scale jets. The reason for this deceleration seems to be the formation of vortices. Where and how are these vortices created ? The possibilities of hydrodynamic instabilities at the head of jets have been discussed before. Norman et al. (1982) discussed that there are Rayleigh-Taylor instabilities at the contact discontinuity. Recently, Krause (2003) mentioned the Kelvin-Helmholtz instability between the flow from hot spot and shocked ambient gas.

To understand the generation of these vortices we need to focus on the flow structure in and around the hot spot. The vortices appear in the hot spot and they originate by the flow through an oblique shock at the end of the beam.

It is known that oblique shocks appear within the beam, even before the end, when the beam expands in lateral directions. This re-establishes pressure equilibrium between the beam and its surroundings and keeps it confined (Fig 6a). When the beam is pinched for some reason, the gas tends to expand due to increased pressure caused by the compression (Fig 6b). If the pressure outside is high enough to confine the beam, an oblique shock appears to prevent it from expansion. (Fig 6c). The radius of the beam after reconfinement depends on the pressure outside of the beam and how the beam is pinched.

Figure 7 shows the rest mass density, pressure and Lorentz factor profile along the z axis of model JB02 at $t = 300, 600, 900, 1200$, and $1500R_b/c$. The beam is confined by the pressure of the cocoon and shocked ambient gas. However the surface of the beam is not

stable. In our calculations the first oblique shock appears where the beam is injected. Such shocks appear irregularly in the beam. As these shocks have different speeds, a slower shock is caught up by a faster shock. This might explain the high emissivity knots in the jets. When an oblique shock appears at the end of the beam, most of the gas passes a terminal Mach shock with large dissipation. However, some of the gas passes through the oblique shocks on the side (Fig. 8 (a)-(b)). If the angle is small, the oblique shock is very weak. The loss of kinetic energy should be small but the pressure becomes as high as that in the cocoon. Then a mildly relativistic back flow begins. The effect of these oblique shocks can be seen in slower jets. This is why the mildly relativistic flow is longer for slower jets. Such a fast velocity flow through the oblique shock can propagate further in lateral direction than slower gas from the hot spot before it propagates backwards. The flow path becomes then a circular, arc like vortex. This vortex can sometimes, which triggers instabilities at the beam surface and internal oblique shocks, reach the beam flow. The surface of the beam becomes more unstable and has oblique shocks there. The oblique shocked flow has an important effect on the gas in the hot spot since it blocks further outflow. In the hot spot the velocity is not constant. The nearer the gas is to a corner that is a crossing point between a contact discontinuity and z axis, the slower the velocity. Although the outflow from the hot spot is blocked, the beam flow continues to enter the hot spot. This then drives a clockwise rotation vortex in the hot spot (Fig. 8 (c)-(e)). This vortex is very important for the dynamics because the increasing radius of vortices causes an increase of cross section of the beam. As a result, the beam decelerates (see Eq.(12)). The vortex can grow till the radius becomes about twice large as that of the beam. The slower a jet is, the larger vortex it can support because the shocked ambient gas which is just going to backward has smaller momentum to this vortex. When a vortex grows, the jet decelerates. On the other hand when a vortex separates (Fig. 8 (f)-(g)), the jet accelerates slightly. But the next vortex grows soon. In Fig. 4 the size of hot spot, namely, the distance between a contact discontinuity and a terminal Mach shock, is oscillating with increasing amplitude. This occurs in all of models but is strongest in the slower jets. The increase of the amplitude of the oscillation increases the growth time of a vortex. A long growth time causes a larger radius of the vortex. The dynamics is a repetition of these processes during the second phase.

Most of gas in this vortex has passed through the 'terminal Mach shock'. The vortex also contains non thermal particles accelerated by this shock. A separating vortex can be observed as an active region around the hot spot. The best candidate for this region is the secondary hot spot discussed in the introduction. The high energy particles lose their energy quickly, so that a separating vortex is a little less bright than that of primary hot spot.

When a jet accelerates, the bow shock has a nose cone like shape. On the other hand,

the bow shock which is decelerating has a flat shape. This may be observed in the eastern lobe of Cygnus A, where the hot spot seems to be slightly ahead of the lobe. This may be because the vortex may just have separated and the jet is in a brief accelerating phase now.

Once a jet exhibits such oblique shocks and vortices, the flow structure around the hot spot becomes more complex. The effect of this turbulence is strong in the case of slowly propagating jets because the confinement effect of shocked ambient gas is weak. The beam is pinched when a circular arc like flow from the oblique shock reaches the beam or a separated vortex moves backwards. The end of the beam tends to expand and has more oblique shocks there. The beam is sometimes constricted in the middle by such effects and a strong shock appears. This shock may be related to knots observed in the beam.

During the later phase of the model JB02, the size of hot spot becomes very large and clumpy. As a result, the gas which passed the terminal Mach shock follows the edge of this clumpy gas. Some of it is mixed in at locations where the gas reaches the shocked ambient gas and back flow begins. This then also separates from the head of the jet and 'normal' hot spot appears again. The large clumpy gas does not display a bright 'hot spot'. It corresponds to a 'temporary absent' hot spot discussed by Saxton, Bicknell, & Sutherland (2003) and can be a good candidate to the absent hot spot in Hercules A.

4.3. SYNCHROTRON EMISSIVITY

Recent some numerical simulations of jets show the surface brightness of the synchrotron emissivity (Scheck et al. 2002; Saxton et al. 2002; Saxton, Bicknell, & Sutherland 2003; Aloy et al. 2003). We follow the analysis by Saxton et al. (2002); Saxton, Bicknell, & Sutherland (2003) and compare our results with theirs and observations.

We use an approximation which assumes the synchrotron emissivity is proportional to $pB^{1+\alpha}$, where p is pressure, B is magnetic field, and α is the spectral index. We use $\alpha = 0.6$ that is typical value. The magnetic pressure $\sim B^2$ is assumed in equilibrium with thermal pressure p . The surface brightness is derived from revolved 2D numerical results. The emissivity is $fp^{1.8}$, where f is the fraction of the gas which originates the beam. The advection equation of f is transformed to conservative form using mass conservation equation and solved with hydrodynamic equations.

Figure 9 and 10 show the emissivity of the models JB02 and JB04 in log scale with four order magnitude from maximum intensity using gray scaled color bar (white is the brightest emissivity) in each panel is shown. Different several angles, $\theta = 0, 15, 30, 45, 60, 75$, and 90° , where θ is the angle between z axis and the line of sight are assumed. JB02 has very extended

emissivity from the head to the root of the jet. On the contrary, JB04 which indicates less complex structure has the emissivity only around the head. Thus, the appearance of vortices causes the extension of emissive regions toward backside. The brightest region corresponds to the hot spot. The other bright regions which corresponds to the oblique shocks in the beam appear irregularly. This may correspond to the observed knots in the beam. The same emissivity is usually seen in the observations of the jets. Both of models have a ring like emissivity near the head of the jet when the angle θ is $30 \sim 75^\circ$. This feature is also shown and discussed the similarity with observation of Hercules A in Saxton et al. (2002); Saxton, Bicknell, & Sutherland (2003). Several rings in the lobe has different radius and emissivity. The observations of Hercules A by Gizani & Leahy (2003) resemble our results of emissivity in JB02. These results indicate that the lobe of Hercules A has a complex structure with vortices.

4.4. RESOLUTION DEPENDENCE

At last, we discuss the dependence of the resolution for our discussion. The calculations with higher resolution allow to have finer structures because how much numerical dissipation is included depends on the resolution. Especially for the problem which has the appearance of vortices, such an effect is very important and may affect the size of vortices and the timing of formations of vortices. We performed calculations with 1.5 times and twice higher resolution for our three cases discussed in the previous sections, but the scales are restricted to save CPU time. In other words 15 (1.5 times resolution) and 20 (twice resolution) grid points are used for innerlet beam.

Higher resolution calculations also show the same property as discussed in the previous subsections, namely, two phases are observed, the jets have the generation and separation vortices at the head of the jet and these effects are strongly seen in the slower injected beam models. Figure 11 shows the time evolution of the positions of the bow shocks, contact surfaces, and terminal Mach shocks with different resolutions for the condition of JB02. This figure is as same as Fig. 4, but only JB02 case is shown and the scales are restricted. The jets with higher resolution propagate a little slower than that of normal version. This is caused by a large separation of a terminal Mach disk from the contact surface in the early second phase because the large separation allows the appearance of large hot spot which is seen in the later phase of the calculation in JB02 with normal resolution and large cross section for the efficiency of the propagation.

5. CONCLUSION

Three numerical simulations of relativistic jets are shown in this paper. We pay special attention to the formation of vortices and its parameter dependence. The propagation velocity derived from one dimensional momentum balance is varied from $0.2c$ to $0.4c$. These estimations for the velocity are based on recent observations of CSOs. We identify two phases based long term simulations, confirming previous results. The propagation velocity during the first phase may be estimated using a one dimensional analysis. The length between the bow shock and the contact discontinuity does not change significantly. On the other hand, the distance between the terminal Mach shock and the contact discontinuity oscillates and its amplitude increases gradually during the second phase. This effect is strongest in slow jets. During the second phase, an oblique shock with a small angle at the end of the beam appears. This flow dramatically affects the dynamics and morphology, and emissivity of the jets in the second phase. Weakly shocked gas then foams a back flow without large energy dissipation. The velocity of this flow is faster than that of expanding flow from the hot spot. The hot spot is blocked by this weakly shocked flow. As a result, a vortex forms in the hot spot. When a vortex grows, the increasing cross section decelerates the jet. When a vortex separates from the jet, the jet accelerates. After this a new vortex appears and this process occurs repeatedly during the second phase. The jet decelerates gradually in time. As a future work, the effect of the generation and separation of vortices at the head of the jet should be investigated using three dimensional numerical simulations.

The synchrotron emissivity of the jets are shown. The strong emissivity of the synchrotron radiation at the hot spot appear. The irregular emissivity on the z axis appears and had same similarity with observed knots in the beam. In the slowest beam model very extended emissivity is shown from the head to the root of the jet and the ring like structure of unusual emissivity of Hercules A is reproduced. In the fastest beam model the emissivity can be seen only around the head of the jet and along the beam. The separation of vortices from the head of the jet strongly affects the extension of the emissivity.

This work was carried out on NEC SX5, Cybermedia Center and Institute of Laser Engineering, Osaka University. We appreciate computational administrators for technical supports.

A.M. acknowledges support from the Japan Society for the Promotion of Science (JSPS). A.M. would like to thank N. Ohnishi, H. Nagatomo, and K. Sawada for useful suggestions to the numerical methods. We also gratefully acknowledge J. M^a. Ibáñez, S. Koide, M. Kino, T. Yamasaki for helpful discussions on AGN jets. We acknowledge comments on the

emissivity by C. Saxton and G. Bicknell. We appreciate useful comments and suggestions by W. van Breugel and anonymous referee which have improved this manuscript.

A. RELATIVISTIC HYDRODYNAMIC CODE

In this appendix, we describe a numerical method used in our relativistic hydrodynamic code and show some results of typical test problems for relativistic hydrodynamic codes, namely, the shock tube problem and strong reflection shock problem.

During the past ten years, numerical methods to solve the relativistic or magneto-relativistic hydrodynamic equations have advanced significantly (see a review paper by Ibáñez & Martí (1999) and references therein). Especially, the method using approximate Riemann solvers provides good accuracy even if the flow includes strong shocks and high Lorentz factors. Recently we have developed a two-dimensional special relativistic code using approximate Riemann solvers which are derived by spectral composition of Jacobian matrices of special relativistic hydrodynamic equations. Plane, cylindrical($r - z$), and spherical($r - \theta$) geometry are assumed.

Recently other new methods also have been employed to relativistic hydrodynamic or relativistic magnetohydrodynamic codes and proposed (Sokolov (2001); Del Zanna & Bucciantini (2002); Anninos & Fragile (2003); Del Zanna, Bucciantini, & Londrillo (2003)).

A.1. NUMERICAL METHOD

Relativistic hydrodynamics equations are written in conservative form in each coordinate system,

PLANE

$$\frac{\partial \mathbf{u}}{\partial t} + \frac{\partial \mathbf{f}(\mathbf{u})}{\partial x} + \frac{\partial \mathbf{g}(\mathbf{u})}{\partial y} = 0, \quad (\text{A1})$$

CYLINDRICAL

$$\frac{\partial \mathbf{u}}{\partial t} + \frac{1}{r} \frac{\partial (r \mathbf{f}(\mathbf{u}))}{\partial r} + \frac{\partial \mathbf{g}(\mathbf{u})}{\partial z} = \mathbf{s}_c(\mathbf{u}), \quad (\text{A2})$$

SPHERICAL

$$\frac{\partial \mathbf{u}}{\partial t} + \frac{1}{r^2} \frac{\partial (r^2 \mathbf{f}(\mathbf{u}))}{\partial r} + \frac{1}{r \sin \theta} \frac{\partial (\sin \theta \mathbf{g}(\mathbf{u}))}{\partial \theta} = \mathbf{s}_s(\mathbf{u}), \quad (\text{A3})$$

where, \mathbf{u} , \mathbf{f} and \mathbf{g} , and \mathbf{s}_c and \mathbf{s}_s are conservative vector, flux vectors, and source vectors, respectively. They are defined as follows,

$$\mathbf{u} = (\rho W, \rho h W^2 v^1, \rho h W^2 v^2, \rho h W^2 - p - \rho W)^T, \quad (\text{A4})$$

$$\mathbf{f}(\mathbf{u}) = (\rho W v^1, \rho h W^2 v^1 v^1 + p, \rho h W^2 v^1 v^2, \rho h W^2 v^1 - \rho W v^1)^T, \quad (\text{A5})$$

$$\mathbf{g}(\mathbf{u}) = (\rho W v^2, \rho h W^2 v^1 v^2, \rho h W^2 v^2 v^2 + p, \rho h W^2 v^2 - \rho W v^2)^T, \quad (\text{A6})$$

$$\mathbf{s}_c = \left(0, \frac{p}{r}, 0, 0\right)^T, \quad (\text{A7})$$

$$\mathbf{s}_s = \left(0, \frac{2p + \rho h W^2 v^2 v^2}{r}, -\frac{\rho h W^2 v^1 v^2 - \cot \theta p}{r}, 0\right)^T. \quad (\text{A8})$$

Then, we disperse these equations for the numerical calculations,

$$\begin{aligned} \mathbf{u}_{i,j}^{n+1} &= \mathbf{u}_{i,j}^n \\ &- \frac{1}{r_{i,j}} \left(r_{i+1/2,j} \tilde{\mathbf{f}}_{i+1/2,j} - r_{i-1/2,j} \tilde{\mathbf{f}}_{i-1/2,j} \right) \frac{\Delta t}{\Delta r_i} \\ &- (\tilde{\mathbf{g}}_{i,j+1/2} - \tilde{\mathbf{g}}_{i,j-1/2}) \frac{\Delta t}{\Delta z_j} \\ &+ \mathbf{s}_{ci,j}, \end{aligned} \quad (\text{A9})$$

where $\mathbf{u}_{i,j}^n$ stands for the average value of \mathbf{u} in the i,j -th grid at t_n , and $\tilde{\mathbf{f}}$ and $\tilde{\mathbf{g}}$ stand for numerical flux through the cell surface. Here, we show the cylindrical coordinate case. Numerical fluxes $\tilde{\mathbf{f}}$ and $\tilde{\mathbf{g}}$ at each cell surface are calculated by Marquina's flux formula derived from left and right eigenvectors and eigenvalues of Jacobian Matrices of relativistic hydrodynamic equations (Donat & Marquina 1996; Donat et al. 1998). To obtain higher accuracy in spatial dimensions, we adopt the MUSCL method (van Leer 1977, 1979) for the reconstruction of the left and right state at each cell surface.

$$(q_L)_{i+1/2} = q_i + \frac{1}{4} \left((1 - \kappa)(\bar{\Delta}_-)_{i+1} + (1 + \kappa)(\bar{\Delta}_+)_{i+1} \right), \quad (\text{A10})$$

$$(q_R)_{i+1/2} = q_{i+1} - \frac{1}{4} \left((1 - \kappa)(\bar{\Delta}_+)_{i+1} + (1 + \kappa)(\bar{\Delta}_-)_{i+1} \right), \quad (\text{A11})$$

where q is the physical value for interpolation. In our code the primitive values such as rest mass density, pressure, and velocity are used for this reconstruction. The accuracy of the code for spatial dimensions is second order when a linear interpolation is adopted ($\kappa = -1$ or, 0), and third order when quadratic function is used for the interpolation ($\kappa = 1/3$). We use minmod limiter to keep Total Variation Diminishing (TVD) condition which prevents the development of numerical oscillations. Then $\bar{\Delta}_+$ and $\bar{\Delta}_-$ are defined;

$$(\bar{\Delta}_+)_{i+1/2} = \minmod(q_{i+1} - q_i, b(q_i - q_{i-1})), \quad (\text{A12})$$

$$(\bar{\Delta}_-)_i = \text{minmod}(q_i - q_{i-1}, b(q_{i+1} - q_i)), \quad (\text{A13})$$

$$\text{minmod}(a, b) \equiv \text{sign}(a) \max(0, \min(|a|, \text{sign}(a) b)), \quad (\text{A14})$$

where b is a parameter that satisfies $1 \leq b \leq (3 - \kappa)/(1 - \kappa)$. The results become diffusive with small b . In this study we use $\kappa = -1$ and $b = 2$. The accuracy of the time-step is first order. Recovery of primitive values from conservative vector \mathbf{u} is done by Newton-Raphson method at every time step (Aloy et al. 1999a).

A.2. TEST CALCULATIONS

We show two types of test calculations of 1-dimensional relativistic hydrodynamics. The calculation is done with a version of 2nd order for space and 1st order for time. 400 grid points in the interested direction are used for both cases. As we assume the dynamics is only one dimensional, the velocity in the other direction is set to be zero initially. So, the velocity of this direction remains zero with time evolution.

A.2.1. SHOCK TUBE PROBLEM

A shock tube problem is a kind of initial value problem. Two states are given between a discontinuity at $t = 0$ initially. This is reasonable because the analytical solution is given by Thompson (1986); Martí & Müller (1994). We use two initial conditions of this problem following Donat et al. (1998).

- Problem 1 : SH1 (Plane)

Left state ($x < 0.5$); $\rho_L = 10, p_L = 13.3, v_L = 0, \gamma_L = 5/3$

Right state ($x > 0.5$); $\rho_R = 1, p_R = 1 \times 10^{-6}, v_R = 0, \gamma_R = 5/3$

- Problem 2 : SH2 (Plane)

Left state ($x < 0.5$); $\rho_L = 1, p_L = 1000, v_L = 0, \gamma_L = 5/3$

Right state ($x > 0.5$); $\rho_R = 1, p_R = 0.01, v_R = 0, \gamma_R = 5/3$

Figures 12 and 13 show the results of these problems at $t = 0.5$ (SH1) and $t = 0.35$ (SH2). Analytical solutions are also shown for the comparison. Despite of more than 5 orders jump in pressure at the initial discontinuity, a rarefaction fan whose front proceeds

towards the left with a sound velocity of the left side state of initial condition, a contact discontinuity and a shock are given with good accuracy in each case except at the density jump behind the shock in SH2.

A.2.2. REFLECTION SHOCK PROBLEM

A reflection shock problem is suitable for studying a flow with a strong shock. Initially a relativistic homogeneous cold flow ($\rho_0, W_0, \epsilon_0 \sim 0$) reflects at $x = 0$; a wall(plane geometry), symmetric axis (cylindrical geometry) or symmetric point (spherical geometry). Then, a strong shock runs against the flow with a high density and pressure jump. Analytical solutions of this problem are given by Rankine-Hugoniot relation of relativistic hydrodynamics (Johnson & McKee 1971).

$$\rho = \left(\frac{\gamma + 1}{\gamma - 1} + \frac{\gamma}{\gamma - 1}(W_0 - 1) \right) \rho_0, \epsilon = W_0 - 1, v = 0, \text{ for } x < V_s t \quad (\text{A15})$$

$$\rho = \rho_0 \left(1 + \frac{|v_0|t}{x} \right)^\alpha, \epsilon \sim 0, v = v_0, \text{ for } x > V_s t, \quad (\text{A16})$$

where V_s is shock velocity,

$$V_s = \left(\frac{W_0 - 1}{W_0 + 1} \right)^{1/2} (\gamma - 1). \quad (\text{A17})$$

The geometry is plane for ($\alpha = 0$), cylindrical ($\alpha = 1$), and spherical ($\alpha = 2$). The expression of rest mass density jump at the shock front is divided in two parts, namely a maximum density compression ratio in non relativistic hydrodynamics ($(\gamma + 1)/(\gamma - 1)$) and including a Lorentz factor.

- Problem 3 : REP

$$\rho_0 = 1.0, \epsilon_0 = 10^{-4}, v_0 = -0.999(W_0 = 22), \gamma = 4/3, \text{ Plane}$$

- Problem 4 : REC

$$\rho_0 = 1.0, \epsilon_0 = 10^{-4}, v_0 = -0.999(W_0 = 22), \gamma = 4/3, \text{ Cylindrical}$$

- Problem 5 : RES

$$\rho_0 = 1.0, \epsilon_0 = 10^{-4}, v_0 = -0.999(W_0 = 22), \gamma = 4/3, \text{ Spherical}$$

Figures 14, 15, and 16 show the numerical results for rest mass density, pressure, and velocity for each of the problems. Analytical solutions are also given. We show the results at $t = 1.57$ when the shock propagates 0.5 from $x = 0$. In all cases the shock front is captured

with good accuracy. Because of numerical problem, a oscillation appears at the front. At the boundary, the error is within 2 % (REP), 6 % (REC), and 5 % (RES) in density. The geometry error in cylindrical and spherical case is 1 % (REC), and 2 % (RES) in density.

REFERENCES

- Aloy, M. A., Ibáñez, J. M^a., Martí, J. M^a., and Müller, E. 1999a, ApJS, 122, 151
- Aloy, M. A., Ibáñez, J. M^a., Martí, J. M^a., Gómez, J. L., and Müller, E. 1999b ApJ, 523, L125
- Aloy, M., Martí, J., Gómez, J., Agudo, I., Müller, E., & Ibáñez, J. 2003, ApJ, 585, L109
- Anninos, P. & Fragile, P. C. 2003, ApJS, 114, 243
- Bahcall, J. N. et al. 1995, ApJ, 452, L91
- Begelman, M. C. & Cioffi, D. F. 1989, ApJ, 345, L21
- Bicknell, G. V. & Wagner, S. J. 2002, accepted for publication in PASA, astro-ph/0204439.
- Biretta, J. A., Sparks, W. B., and Macchetto, F. 1999, ApJ, 520, 621
- Blandford, R. D. and Rees, M. J. 1974, MNRAS, 169, 395
- Carilli, C. L. & Barthel, P. D. 1996, A&A Rev., 7, 1
- Carilli, C. L., Perley R., Harris, D. E, & Barthel, P. D. 1998, Phys. Plasmas 5, 1981
- de Gouveia Dal Pino, E. M. 1999, ApJ, 526, 862
- Del Zanna, L. & Bucciantini, N. 2002, A&A, 390, 1177
- Del Zanna, L., Bucciantini, N., & Londrillo, P. 2003, A&A, 400, 397
- Donat, R., & Marquina, A. 1996, J. Comput. Phys., 125, 42
- Donat, R., Font J. A., Ibáñez, J. M^a., and Marquina, A. 1998, J. Comput. Phys., 146, 58
- Duncan, G. C. and Hughes, P. A. 1994 ApJ, 436, L119
- Eulderink, F. and Mellema, G. 1995, A&AS, 110, 587
- Ferrari, A. 1998, ARA&A, 36, 539

- Font, J. A., Ibáñez, J. M^a., Marquina, A. and Martí, J. M^a. 1994, A&A, 282, 304
- Giroletti, M., Giovannini, G., Taylor, G. B., Conway, J. E., Lara, L., & Venturi, T. 2003, A&A, 399, 889
- Gizani, N. A. B., & Leahy, J. P. 2003, MNRAS, 342, 399
- Hughes, A. H., Miller, A. M., & Duncan, G. C. 2002, ApJ, 572, 713
- Ibáñez, J. M^a., and Martí, J. M^a. 1999, J. Comput. Appl. Math., 109, 173
- Jester, S., Roser, H.-J., Meisenheimer, K., and Perly, R. 2002, A&A, 385, L27
- Johnson, M. H., and McKee, C. F. 1971, PRD, 3, 858
- Kataoka, J., Edwards, P., Georganopoulos, M., Takahara, F., and Wanger, S. 2003, A&A, 399, 91
- Koide, S., Shibata, K., Kudoh, T., & Meier, D. L. 2002, Science, 295, 1688
- Koide, S., Nishikawa, K., Mutel, R. L. 1996, ApJ, 463, L71
- Komissarov, S. S. 1999, MNRAS, 303, 343
- Komissarov, S. S. 1999, MNRAS, 308, 1069
- Kraft, R. P. et al., 2002, ApJ, 569, 54
- Krause, M. 2003, A&A, 398, 113
- Landau, L. D., and Lifshitz, E. M. 1987, Fluid Mechanics (Second Edition), Pergamon press.
- Livio, M. 1999, Phys. Rep., 311, 225
- Marshall, H. L., et al. 2001, ApJ, 549, L167
- Marshall, H. L., et al. 2002, ApJ, 564, 683
- Martí, J. M., and Müller, E. 1994, J. Fluid Mech., 258, 317
- Martí, J. M., Müller, E., Font, J. A., Ibáñez, J. M^a., and Marquina, A. 1997, ApJ, 479, 151
- Martí, J. M., Müller, E., & Ibáñez, J. M. 1998, Astrophysical Jets: Open Problems, 149
- Norman, M. L., Winkler, K.-H. A., Smarr, L. and Smith, M. D. 1982, A&A, 113, 285

- Norman, M. L., Winkler, K. H. A., & Smarr, L. 1983, ASSL Vol. 103: Astrophysical Jets, 227
- Owsianik, I., and Conway, J. E. 1998, A&A, 337, 69
- Pearson, T. J., et al. 1981, nature, 290, 365
- Polatidis, A. G., and Conway, J. E. 2003, Publications of the Astronomical Society of Australia, 20, 69
- Rosen, A., Hughes, P. A., Duncan, G. C., & Hardee, P. E. 1999, ApJ, 516, 729
- Sambruna, R. M., et al. 2001, ApJ, 549, L161
- Sambruna, R. M., et al. 2002, ApJ, 571, 206
- Saxton, C. J., Sutherland, R. S., Bicknell, G. V., Blanchet, G. F., & Wagner, S. J. 2002, A&A, 393, 765
- Saxton, C. J., Bicknell, G. V., & Sutherland, R. S. 2002, ApJ, 579, 176
- Scheck, L., Aloy, M. A., Martí, J.M^a., Gómez, J. L., and Müller, E. 2002 MNRAS, 331, 615
- Scheuer, P. A. G. 1974, MNRAS, 166, 513
- Sokolov, I. V., Zhang, H.-M., & Sakai, J. I. 2001, J. Comp. Phys., 171, 209
- Spada, M., Ghisellini, G., Lazzati, D., & Celotti, A. 2001, MNRAS, 325, 1559
- Thompson, K. W. 1986, J. Fluid Mech., 171, 365
- van Leer, B. 1977, J. Comput. Phys., 23, 276
- van Leer, B. 1979, J. Comput. Phys., 32, 101
- Wilson, A. S., Yang, Y., and Shopbell, P. L. 2000, ApJ, 544, L27
- Wilson, A. S., and Yang, Y. 2002, ApJ, 568, 133
- Zhang, H., Koide, S., & Sakai, J. 1999, PASJ, 51, 449

| | JB02 | JB03 | JB04 |
|-----------------------------|-----------------------|-----------------------|-----------------------|
| $\eta \equiv \rho_b/\rho_a$ | 1.28×10^{-3} | 3.76×10^{-3} | 9.15×10^{-3} |
| $M_b \equiv v_b/c_b$ | 6.0 | 6.0 | 6.0 |
| ϵ_b | 2.55×10^{-2} | 2.55×10^{-2} | 2.55×10^{-2} |
| γ | 5/3 | 5/3 | 5/3 |
| $K \equiv p_b/p_a$ | 10 | 33 | 100 |
| $W_b(v_b)$ | 7.1(0.99) | 7.1(0.99) | 7.1(0.99) |
| v_j^{1D} | 0.2 | 0.3 | 0.4 |
| expiration time $R_b/(c)$ | 1800 | 1200 | 600 |

Table 1: numerical conditions of models

Fig. 1.— Contours of rest mass density(top), pressure(middle), and Lorentz factor(bottom) of model JB02 at the end of the simulation ($t = 1770[R_b/c]$)

Fig. 2.— Contours of rest mass density(top), pressure(middle), and Lorentz factor(bottom) of model JB03 at the end of the simulation ($t = 1140[R_b/c]$)

Fig. 3.— Contours of rest mass density(top), pressure(middle), and Lorentz factor(bottom) of model JB03 at the end of the simulation ($t = 570[R_b/c]$)

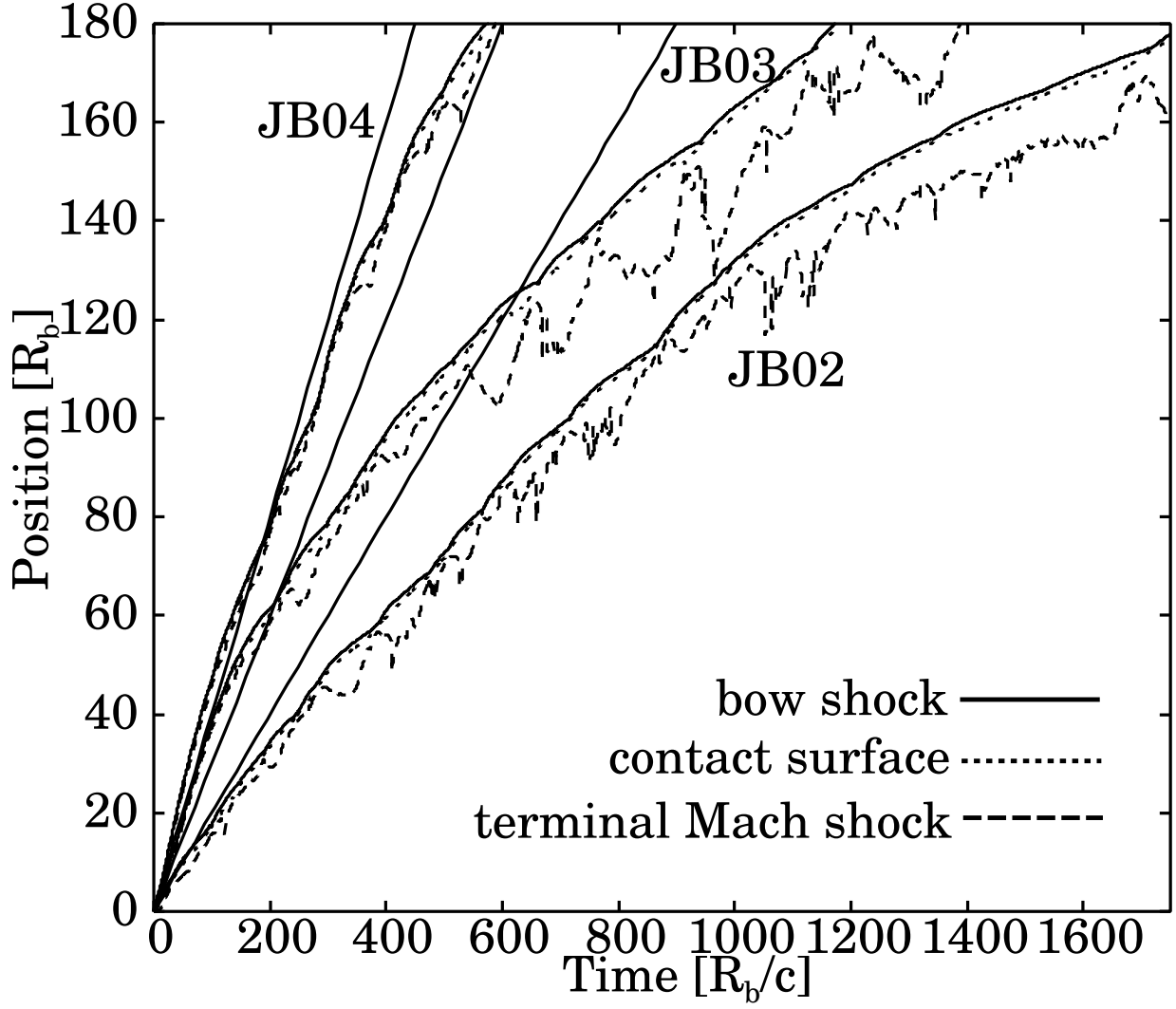


Fig. 4.— Time evolution of the position of the bow shock, the contact discontinuity, and the terminal Mach shock for models JB02, JB03 and JB04.

Fig. 5.— The absolute velocity ($r > 0$) and log scale rest mass density contour ($r < 0$) of model JB02 (top), JB03 (middle), and JB04 (bottom) in early phase, at $t = 107.5R_b/c$ (JB02), $t = 50.0R_b/c$ (JB03), $t = 35.0R_b/c$ (JB04)

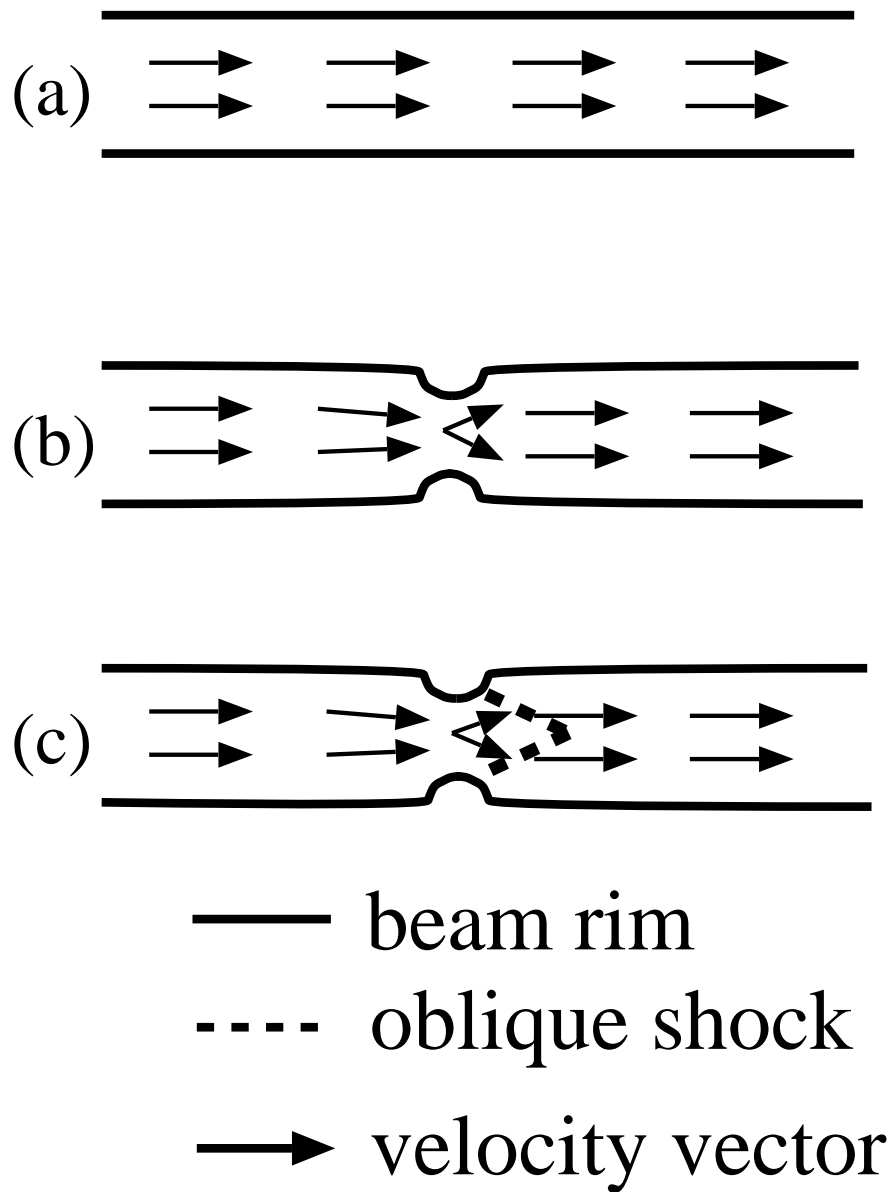


Fig. 6.— A schematic of appearance of an oblique shock in the beam (not scaled)

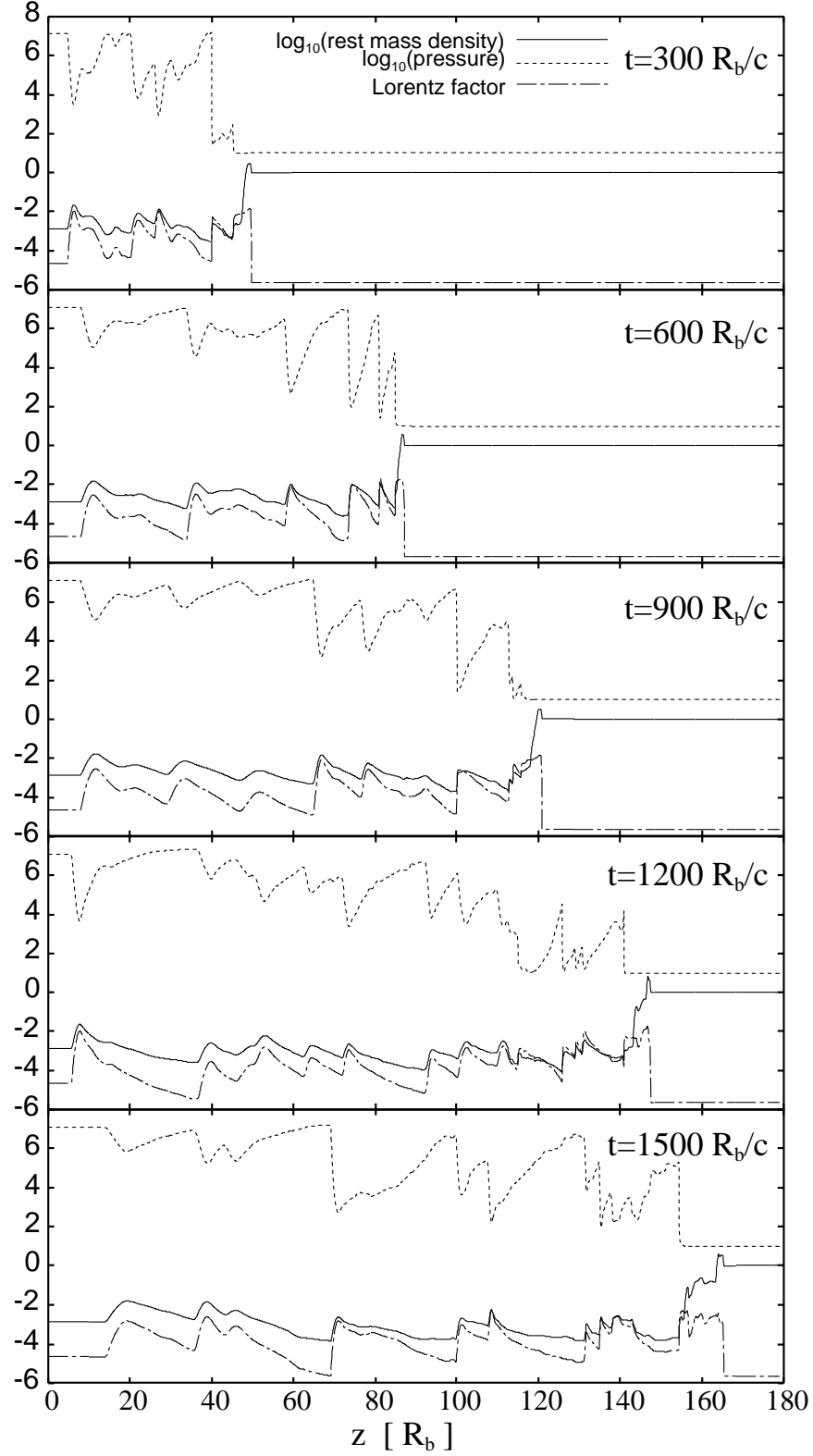


Fig. 7.— The log scale rest mass density (solid), log scale pressure (dashed), and Lorentz factor (dashed point) profile along the z axis of model JB02 at $t=300, 600, 900, 1200$, and $1500 R_b/c$.

Fig. 8.— A series of profiles of growing and separating of vortices. In each panel the top shows the absolute velocity $r > 0$ and the bottom shows rest mass density $r < 0$, (a):normal profile, (b):an oblique shock appears, (c)-(e):a vortex grows up a vortex, (f)-(g):separates from top of the jet

Fig. 9.— Synchrotron emissivity of JB02 at $t = 1770[R_b/c]$ with several angle $\theta = 0, 15, 30, 45, 60, 75$, and 90° , where θ is the angle between z axis and the line of sight. Counters are shown in log scale with four order magnitude from maximum intensity using gray scaled color bar (white is the highest emissivity) in each panel.

Fig. 10.— Same as Fig. 9 of JB04 at $t = 570[R_b/c]$.

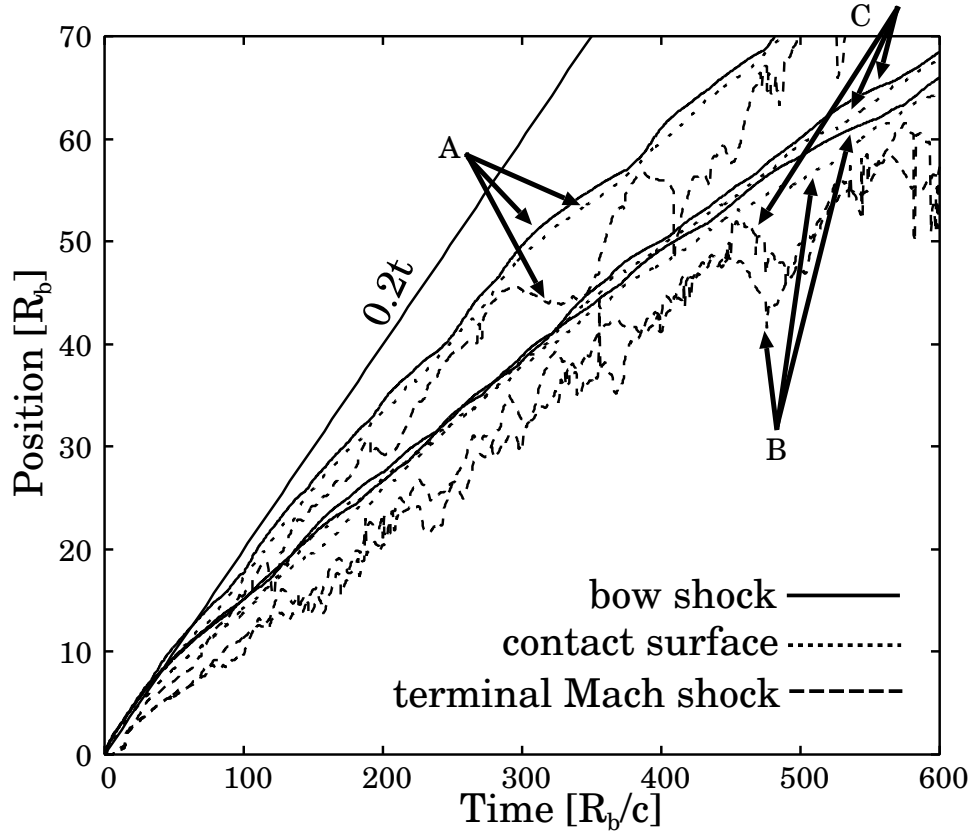


Fig. 11.— Time evolution of the surfaces at the head of the jets (same as 4 but only JB02) using different resolution for the calculation. A (innerlet beam 10:normal case), B (15), C(20).

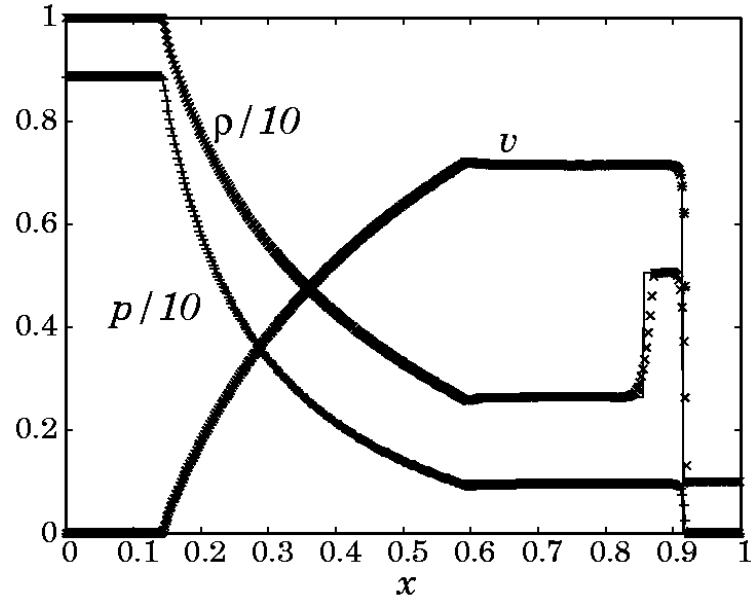


Fig. 12.— Test calculation of shock tube problem (SH1), rest mass density (ρ), pressure (p), velocity (v) are shown at $t=0.5$. Initial discontinuity is at $x = 0.5$. Solid lines are analytical solutions.

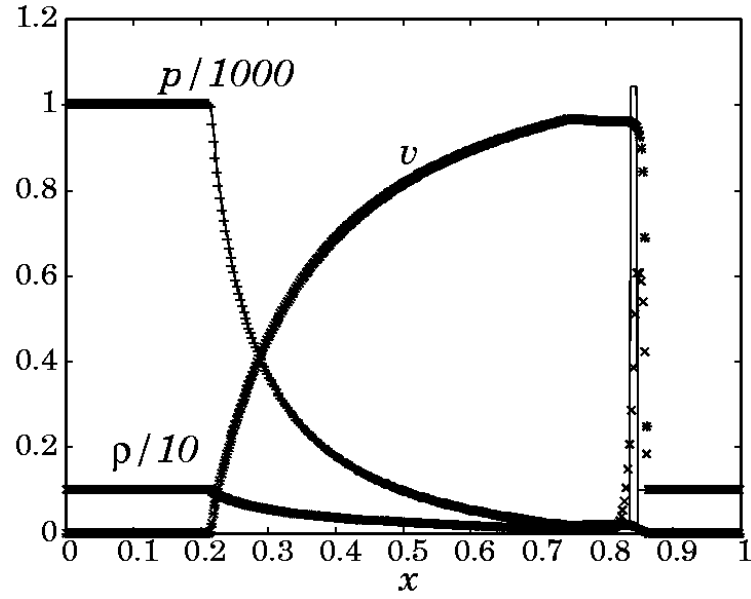


Fig. 13.— Same as Fig. 12 of SH2 at $t = 0.35$.

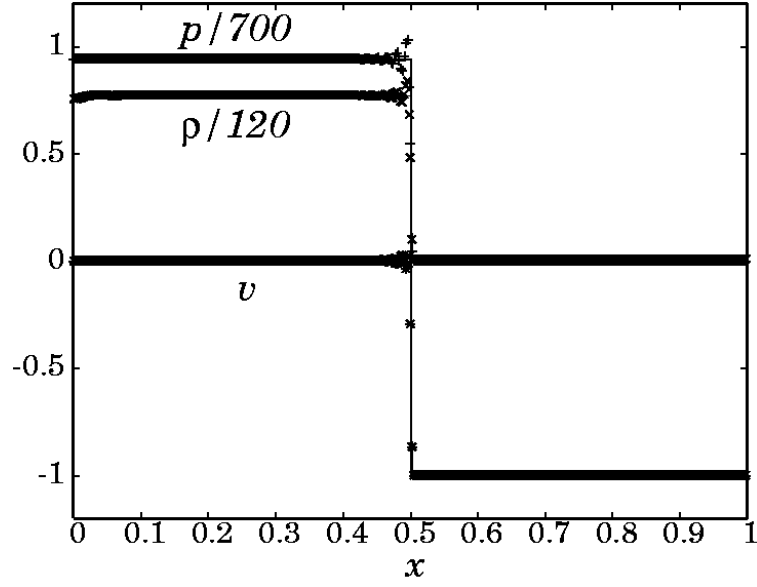


Fig. 14.— Test calculation of reflection shock problem (REP;plane), rest mass density (ρ), pressure (p), velocity (v) are shown at $t=1.57$. Solid lines are analytical solutions.

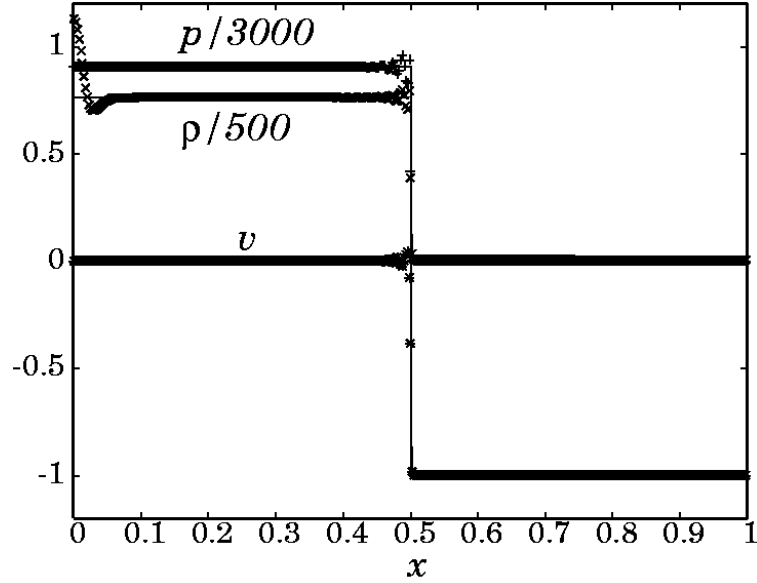


Fig. 15.— Same as Fig. 14 of REC(cylindrical) at $t = 1.57$.

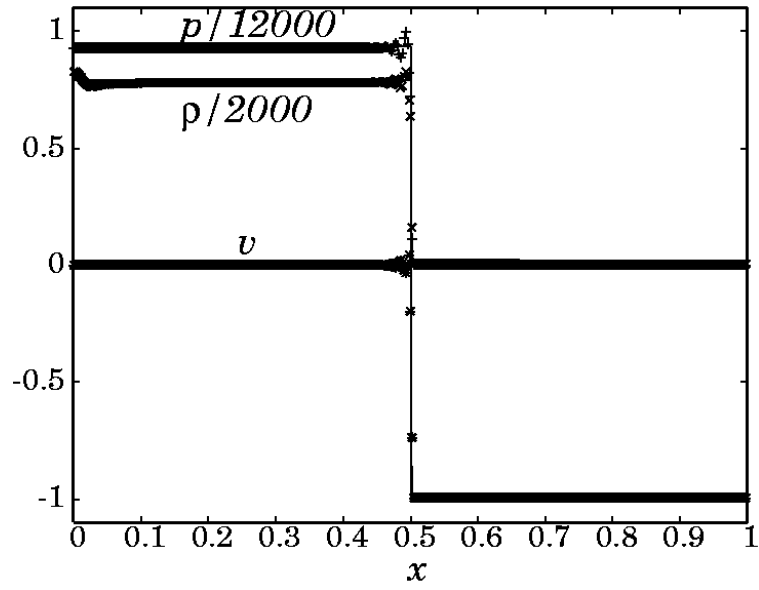


Fig. 16.— Same as Fig. 14 of RES(spherical) at $t = 1.57$.

This figure "fig1mod.jpg" is available in "jpg" format from:

<http://arxiv.org/ps/astro-ph/0402355v1>

This figure "fig2mod.jpg" is available in "jpg" format from:

<http://arxiv.org/ps/astro-ph/0402355v1>

This figure "fig3mod.png" is available in "png" format from:

<http://arxiv.org/ps/astro-ph/0402355v1>

This figure "fig5_mod.jpg" is available in "jpg" format from:

<http://arxiv.org/ps/astro-ph/0402355v1>

This figure "fig8mod.jpg" is available in "jpg" format from:

<http://arxiv.org/ps/astro-ph/0402355v1>

This figure "fig9.jpg" is available in "jpg" format from:

<http://arxiv.org/ps/astro-ph/0402355v1>

This figure "fig10.jpg" is available in "jpg" format from:

<http://arxiv.org/ps/astro-ph/0402355v1>